communications materials

Article

https://doi.org/10.1038/s43246-024-00485-5

Light-driven anisotropy of 2D metal-organic framework single crystal for repeatable optical modulation

Yuliya A. Kenzhebayeva[1,10], Nikita K. Kulachenkov[1,9,10], Sergey S. Rzhevskiy[1], Pavel A. Slepukhin[2], Vladimir V. Shilovskikh[3], Anastasiia Efimova[1], Pavel Alekseevskiy[1], Gennady Y. Gor[4], Alina Emelianova[4], Sergei Shipilovskikh[1], Irina D. Yushina[5], Alexander Krylov[6], Dmitry I. Pavlov[7], Vladimir P. Fedin[7], Andrei S. Potapov[7] ✉ & Valentin A. Milichko[1,8] ✉

Structural transformations of metal-organic frameworks (MOFs) go through a complex energy landscape with multiple intermediate states. Although the transformations allow controlling the functional properties of the MOFs, an imbalance between MOF flexibility and rigidity sets a fundamental barrier to achieving fast and multiple transformations. Here, we study the stimuli-responsive structural transformation in a 2D MOF assembled from paddle-wheel secondary building units joined by a semi-flexible organic ligand with 1,2,4-triazole and carboxylate groups with a rigid adamantane cage between them. The structure results in a distinctive combination of MOF flexibility and rigidity, thus, facilitating a continuous transformation driven by laser light. We reveal the laser-induced anisotropic thermal expansion nature of such transformation, initiating optical changes of the 2D MOF. The latter is utilized for fast and highly repeatable optical modulation of over 10,000 cycles. The endurance of such a 2D MOF-based optical modulator during 1 year of storage at ambient conditions paves the way to design tunable and robust MOFs for diverse applications.

Metal-organic frameworks (MOFs), as part of a large family of coordination polymers, have emerged as a unique class of porous crystalline materials for diverse applications ranging from engineering chemistry to catalysis and even nonlinear optics. In contrast to rigid and kinetically stable MOFs[1–3], demonstrating the structural resistance at harsh conditions to a certain extent[2], their flexible (soft, dynamic, adaptive, or four-dimensional) counterparts[4–8] imply diverse structural transformations (STs)[9–12] upon the guest uptake, elevated pressure and/or temperature, and applied electromagnetic fields[13–16]. On the one hand, such transformations offer an efficient route to control the gas/solvent separation and sorption properties of MOFs[17–19]. On the other hand, controllable STs bring the flexible MOFs into a list of smart materials for diverse applications[4,15,20,21].

In terms of solid state physics, STs of most MOFs can be classified as phase transitions[22–30], breathing, thermal expansion, and even defect formation[20,31] accompanied by the ligand dynamics[26], conformations[27–29], to the chemical bonds rearrangement and breaking[30]. Moreover, due to the complex composition and the framework hierarchy, the STs may be associated with a change in the space group (and/or crystal symmetry)[9], or occur at a fixed MOF structure[13]. As a result, STs determine the changes of chemical, electronic, magnetic, and mechanical properties of the MOFs[31,32]. However, the STs of most stimuli-responsive MOFs are described generally by a limited number of cycles and a relatively low rates (from hours to milliseconds), being a consequence of the reasons including weak intermolecular forces (preventing the return of MOF structure to its initial state) and complex multi-step ST paths.

[1]School of Physics and Engineering, ITMO University, St Petersburg 197101, Russia. [2]Postovsky Institute of Organic Synthesis, Ural Branch of the Russian Academy of Sciences, Ekaterinburg 620137, Russia. [3]Center for Advancing Electronics, Technische Universität Dresden, 01069 Dresden, Germany. [4]Otto H. York Department of Chemical and Materials Engineering, New Jersey Institute of Technology, University Heights, Newark, NJ 07102, USA. [5]South Ural State University, Chelyabinsk 454080, Russia. [6]Kirensky Institute of Physics, Federal Research Center KSC SB RAS, Krasnoyarsk 660036, Russia. [7]Nikolaev Institute of Inorganic Chemistry SB RAS, Novosibirsk 630090, Russia. [8]Institut Jean Lamour, Universit de Lorraine, UMR CNRS 7198, 54011 Nancy, France. [9]Present address: Tufts University, Boston, MA 02155, USA. [10]These authors contributed equally: Yuliya A. Kenzhebayeva, Nikita K. Kulachenkov. ✉e-mail: potapov@niic.nsc.ru; v.milichko@metalab.ifmo.ru

Here, we report on a two-dimensional (2D) MOF assembled from incomplete (i.e., containing three carboxylate bridges instead of four)[33] paddle-wheel secondary building units (SBU), joined by a semi-flexible organic ligand with 1,2,4-triazole and carboxylate groups with a rigid adamantane cage between them[34]. Such structure results in a distinctive combination of the framework flexibility and endurance due to allowed deformations of the ligand shape and SBU in a reversible manner. It, thus, facilitates a continuous ST, driven by low-intensity laser light. In situ optical, mechanical, numerical, and structural analysis reveal that such ST is a laser-induced thermal expansion process accompanied by reversible anisotropic spatiotemporal volume expansion. We also confirm that the ST initiates the change in optical properties of 2D MOF along orthogonal directions, utilized then for fast (5000 s^{-1}) and highly repeatable (over 10^4 cycles of ST) optical modulation. The latter is expressed as a rotation of the polarization of the transmitted visible light. The reported endurance and structural resistance (during 1 year of storage at ambient conditions) of such 2D MOF-based optical modulator pave the way to design a series of tunable and robust MOFs for diverse chemical and optical applications.

Results and discussion

Design

To address the challenge of multiple and fast STs of MOFs with low energy consumption, we refer to the experimentally discovered Barker rule for solids[35]. According to that rule, there is a relation between an elastic modulus E and thermal expansion coefficient α of a solid ($E \cdot \alpha^2 \sim$ const): the more flexible the solid (low value of E), the greater the α and, hence, physicochemical properties of the corresponding solid can be changed more efficiently with less energy consumption[36]. However, for the rigid solid (high value of E and low value of α), faster and less efficient changes of the solid' properties can be detected. Thus, there is a contradiction: if someone needs to achieve a higher ST rate (κ), the structure of the corresponding solid provides weaker changes in its physicochemical properties, which strongly limits the real-life application. Therefore, we assume that fast (i.e., high κ), multiple (due to high E), and simultaneously efficient ST (corresponding to high value of α) can be precisely achieved through the balance between the MOF flexibility and its volume expansion.

In this sense, we rationally designed and synthesized 2D MOF (**1**) based on copper(II) cations and a hybrid angle-shaped 1,2,4-triazole-carboxylate ligand with a rigid cage hydrocarbon (adamantane) linker (Fig. 1a, b)[37]. In the structure of **1**, two Cu^{2+} cations are linked by three bridging carboxylic groups of the ligand into an incomplete paddle-wheel SBU (Fig. 1c)[33]. The apical positions of the SBU are occupied by the nitrogen atoms of 1,2,4-triazole rings of two different ligands. Instead of the fourth carboxylate group in a typical paddle-wheel SBU, the two remaining coordination places of two Cu^{2+} cations are occupied by an additional nitrogen atom of the ligand and an oxygen atom of the coordinated methanol molecule. Overall, the SBU is six-connected and these units are joined into 2D layers oriented parallel to the crystallographic bc plane (Fig. 1d, e).

Structural transformation

Based on the structural data, we have performed in advance the molecular modeling (see Supplementary Note 4), which revealed the following. When the heating of the structure of **1** is initiated by 10 K, a linear increase in the total energy occurs with a slope of 2.92 kJ mol^{-1} K^{-1} (Supplementary Fig. S6a), associated with 10 to 20 % change in the angles of both the coordination bond (Cu-O-C, O-C-O, and O-C-C) and the ligand (N-N-C, and N-C-C, Supplementary Fig. S6b). To confirm the predicted transformations of **1**, we have performed in-situ powder and single crystal X-Ray diffraction analyses with a heating mode (PXRD in Fig. 1f, and SCXRD in Supplementary Note 2). As one can see in Fig. 1f, the PXRD pattern demonstrates the continuous[12,38] (from 298 to 338 K) and reversible ST, associated with the anisotropic volume expansion up to 1% at a fixed space group $P2_1/c$ of **1**. Thermogravimetric measurements (TGA, see Supplementary Fig. S4) also confirmed the continuous behavior of the ST of **1**. The detailed SCXRD analysis over heating (Fig. 1e, Supplementary Tables S1–S3, and Supplementary Figs. S1–S3) revealed the reversible changes in the coordination bonds and the ligand shape, being in a qualitative agreement with the molecular modeling results: the covalent bonds in the ligand, as well as the coordination bonds in Cu^{2+} coordination sphere did not change within the experimental error (Supplementary Table S4). In contrast, the torsion angles corresponding to the rotation of the carboxylate and 1,2,4-triazole groups relative to the rigid adamantane linker, as well as the bond angles in metal coordination sphere changed notably upon heating from 298 to 338 K (Fig. 1e, Supplementary Fig. S1, and Supplementary Table S4). These changes led to distortion of the SBU, evident from elongation of Cu-Cu interatomic distance. We assumed that this distortion has been facilitated by incompleteness of the paddle-wheel SBU (three carboxylate bridges instead of four). Herein, the characteristic Cu-Cu internuclear distance within these SBUs increased monotonously and linearly in 298–338 K temperature range (Supplementary Fig. S3f). The orientation of the SBUs in the unit cell led to stretching of 2D MOF layers along the crystallographic axis c and their separation along the crystallographic axis a during the ST (Supplementary Fig. S2). All these movements of the structure of **1** upon heating are reflected in the simulated video (Supplementary Video 1). It is important that the individual crystals of **1** demonstrated the volume expansion ranging from 0.5 to 0.9 % (Supplementary Table S3) under the same heating conditions, which can be associated with the imperfection of the synthesized MOFs.

In addition to the structural analysis, we have performed a study of low-energy vibrations of the MOF structure (associated with changes of the structure as a whole) upon heating. Experimental results and modeling (Supplementary Fig. S27) also confirmed that the heating of **1** by tens of Kelvins led to changes in the vibration energies associated with conformations of triazole and adamantane units (Supplementary Table S13). The latter indirectly confirms the results of molecular modeling, TGA, PXRD, and SCXRD and allows us to refer the observed ST to a thermal expansion. Therefore, using the results of SCXRD over heating (Supplementary Tables S1–S4), we have estimated the thermal expansion coefficient, α, of **1** ($221.4 \cdot 10^{-6}$ K^{-1}, see Table 1 and Supplementary Table S5), which has been appeared in the gap between flexible and fairly rigid MOFs (Supplementary Table S6).

Staying in the paradigm of the balance between E and α, we have also analyzed experimentally and numerically the mechanical properties of single crystals of **1** (see Supplementary Notes 5, 6): The determined value of Young's modulus E (the calculated value of 17 ± 2 GPa, and the experimental one ranging from 4.6 to 72 GPa, depending on the atomic force microscopy approach) places **1** again between flexible and fairly rigid MOFs (Supplementary Table S9). In addition, atomic force microscopy before and during the ST has also confirmed the effect of thermal expansion of **1**: As can be seen in Supplementary Fig. S10, continuous irradiation of the single crystal of **1** by laser light (800 nm, 12 mW integral power corresponding to 10^5 W cm^{-2} power density) led to a reversible 4 ± 1 % increase in its thickness, being larger than the structural data reported (Supplementary Table S1-S3) probably due to the stronger heating of **1** (see Supplementary Note 5).

Dynamics

Next, to reveal the ST rate, κ, we have assumed that the thermal expansion of **1** is independent on the source of heating. Thus, we have checked the ST upon the laser-induced heating by the wavelength providing an effective absorption of light by **1** and conversion of the photon energy to the heat (Supplementary Fig. S16a)[13]. In situ SCXRD and PXRD with the laser mode (Supplementary Fig. S5 and Supplementary Table S7) confirmed that, upon the action of continuous laser irradiation (800 nm wavelength, 12 mW integral power corresponding to $2 \cdot 10^3$ W cm^{-2} power density), **1** demonstrated similar reversible anisotropic volume expansion, as has been detected upon conventional heating (Supplementary Table S1–S3). The similarity is described within the error in determining the lattice parameters (Supplementary Tables S2, S7) and the individuality of each single crystal

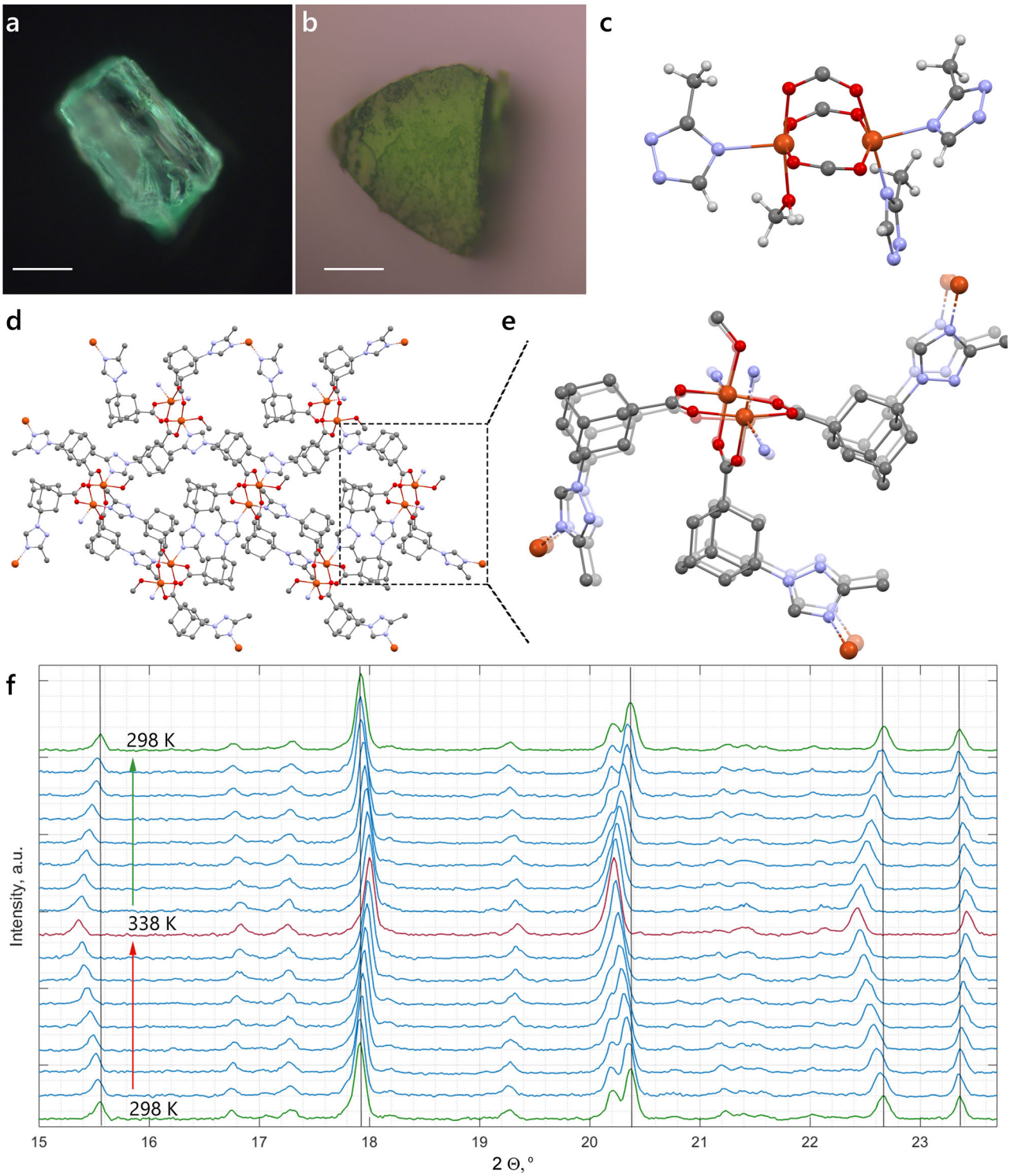

Fig. 1 | Crystal structure of 1. Optical images of the single crystal of **1** in dark and bright fields. Scale bars, 50 μm (**a**) and 100 μm (**b**). **c** Secondary building unit of **1**, adamantane fragments are omitted for clarity and (**d**) the layer of **1**, viewed along the crystallographic axis *b* (hydrogen atoms and nitrate anions are omitted for clarity). Color code: gray—carbon, light-gray—hydrogen, blue—nitrogen, red—oxygen, orange—copper. **e** The structural transformation of **1** extracted from SCXRD analysis upon heating (see Supplementary Fig. S1). **f** In-situ PXRD patterns (CoK_α radiation) recorded upon the heating of the powder of **1** from 298 to 338 K with 5 K step.

(Supplementary Table S3). Based on this data, we have then utilized an optical pump-probe spectroscopy to indirectly reveal the κ value[39,40]: As a pump, the laser pulses of near-infrared region (800–1100 nm, Supplementary Fig. S16a) are considered as a heating source; while as a probe, the laser pulses, sensitive to the structure-related electronic (optical) changes of **1** and non-perturbing its structure[14], should be utilized. Therefore, to select the optimal wavelength of the probing laser pulses, we have measured the transmission optical spectra of single crystal of **1** before and during the ST. As one can see in Fig. 2a, the ST induced by the laser-induced heating (by 800 and 1050 nm) or conventional heating on Peltier stage (see also Supplementary Fig. S17) is accompanied by similar 12 nm spectral shift within the whole visible ranges. Supplementary Fig. S16b shows in detail

(through the ratio of the transmission optical spectra of **1** before and during the ST) that wavelengths from 410 to 750 nm can be considered as probing, and then we indicated 600 nm as an optimal one.

Thus, utilizing a low-intensity of 600 nm laser pulses (6 ns) as a probe, and a single 1060 nm laser pulse (100 ns) as a pump, we have discovered the following. The ST (i.e., thermal expansion led to the transmission spectral shift from the initial to the excited state) occurs over $\tau \sim 0.2$ ms (the rate $\kappa \sim 1/\tau \sim 5000\ s^{-1}$) with 3.3 ms relaxation (Fig. 2b), being equal or even greater than that of specific photosensitive MOFs. In details, the laser-induced heating led to the volume expansion and initiated a decrease in the intensity of the transmitted probe pulse due to the drop of the MOF transmittance at 600 nm (Fig. 2a and Supplementary Fig. S16b); while the relaxation of the structure of **1** to the initial state (corresponding to the structure at 298 K, Supplementary Table S1) returned the probe intensity to its initial value. Intriguing is that the variation of the wavelength of the probing light from 500 to 750 nm revealed the opposite behavior of its intensity (Supplementary Fig. S21a): The decline followed by the growth of the intensity of 500–650 nm light over time is due to the fact that these wavelengths can be efficiently absorbed by **1** during the ST; while the growth followed by the decline of the intensity of 700–750 nm light can be explained by an increase of transparency of **1** within this spectral range during the ST (Supplementary Fig. S16b). In addition, these results revealed that an increase in excitation time from 0.15 to 0.2 ms and the relaxation time from 1 to 4.5 ms correlated with the decrease of the probe wavelengths from 750 to 500 nm. This allowed us to determine an average 3.8 ms time required to complete the ST process, and to speculate about app. 260 full cycles of the reversible STs of **1** per second.

It is worth noting that a comparison of the data obtained (in situ SCXRD in heating mode and the laser-induced heating) indicated that the heating of **1** from 298 to 338 K provided 1% volume change (Supplementary Table S1–S3). The same temperature range led to 5 nm spectral shift for **1**, heated on Peltier stage (Supplementary Fig. S17d), allowing us to determine an efficiency of the optical changes upon heating (0.125 nm K^{-1}). The latter has been used then for evaluating the heating of MOF directly by the laser (Fig. 2a, inset): the same 5 nm spectral shift, achieved with 3.5 mW of the laser power, can be attributed also to 338 K of **1** achieved by the laser-induced heating.

Table 1 | Operation and physical parameters of 1

Thermal expansion coefficient, α_V	Young's modulus, E	Rate of ST, κ	Number of ST cycles
$221.4 \cdot 10^{-6}\ K^{-1}$	4.62[a] (17 ± 2)[b] GPa	$5000\ s^{-1}$	10^4

[a]Experiment.
[b]Theory.

Endurance

For such 2D MOF demonstrating E vs α balance and relatively high thermal expansion rates, we have checked its endurance at ambient conditions (air atmosphere, room temperature and humidity) during the ST cycles stimulated by the laser-induced heating (1050 nm, 7.2 mJ cm^{-2} laser fluence). Figure 2c shows that the single crystal of **1** demonstrates unprecedented endurance during 10^4 cycles of the ST expressed as 6 nm shift of the optical transmission of **1** (corresponding to heating to 348 K). A slight 2 nm shift, observed between 1500 and 4000 cycles, is probably related with the

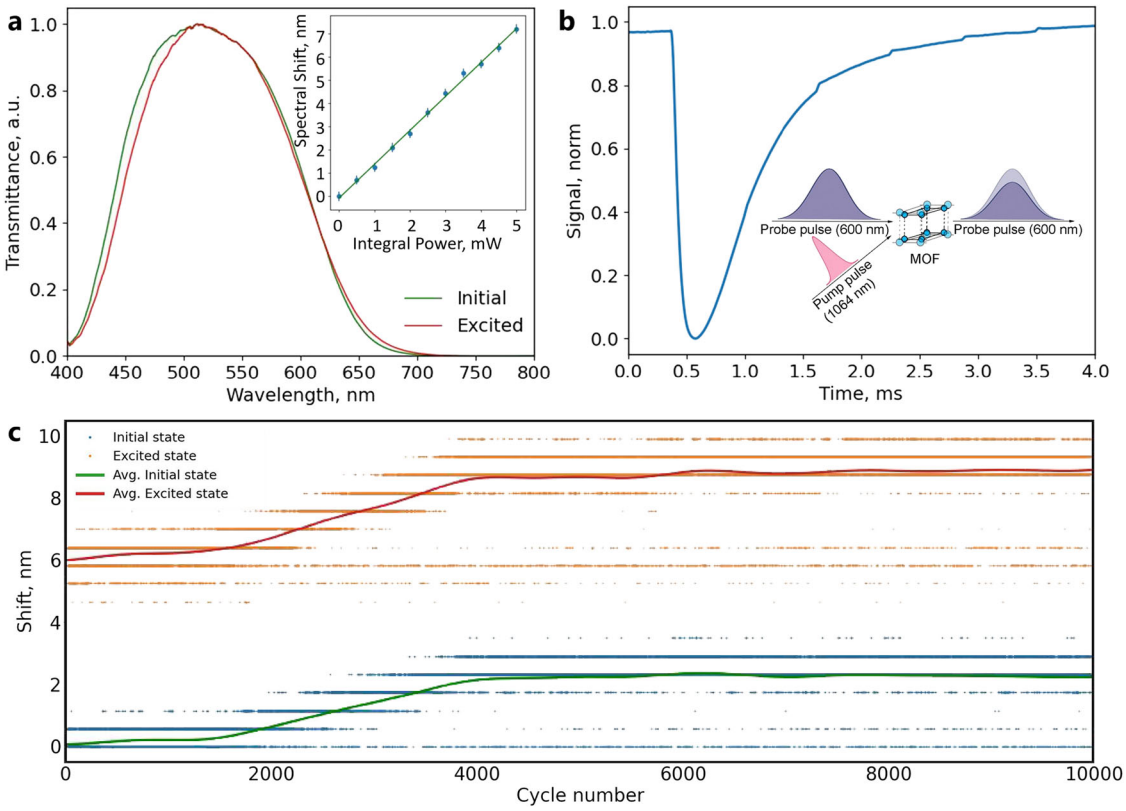

Fig. 2 | The dynamics of the structural transformation of 1. a The normalized optical transmission spectra of the single crystal of **1** before (initial state, green curve) and during the ST (excited state, red curve), stimulated by laser heating (1050 nm, 150 fs). Inset: linear dependence of the spectral shift on the pumping laser power. **b** The dynamics of the ST expressed as the evolution of the intensity of 600 nm probing laser light passing through the single crystal of **1** during the ST, stimulated by a single laser pulse (1064 nm, 100 ns pulse duration). Inset: the scheme of the laser pump-probe spectroscopy. **c** Long-term stability of single crystal of **1** at ambient conditions (air atmosphere, room temperature and humidity) during 10^4 cycles of the ST, stimulated by laser-induced heating (1050 nm as a pump with a fluence of 3.6 mJ cm^{-2}; and 600 nm as a probe). Green curve—initial state; red curve—excited state (during the ST).

removing of residual solvent molecules (coordinated methanol, see TGA in Supplementary Fig. S4a). Surprisingly, such relatively fast and multiple (10^4 cycles) ST has been also confirmed for single crystals of **1** in 1 year of storing at ambient conditions (Supplementary Fig. S25). Coupled with SCXRD data on reversible ST (3 cycles, see Supplementary Table S2), these results unambiguously addressed the question of the possibility of simultaneous coexistence of the structural flexibility and integrity of the MOF (Table 1).

Notably, the observed continuous ST (i.e., thermal expansion) of **1** with movable elements (SBU and ligand), on the one hand, initiated the detectable optical changes with the rate of app. 5000 s^{-1}; on the other, was accompanied with the MOF structural integrity confirmed by 10^4 ST cycles. The latter value exceeds all previously declared cycles of the transformation of the flexible MOF, bringing, thus, the reported compound closer to the rigid one, subjected to alternating electric field over thousands of cycles for semi-commercial capacitive and memory elements[31,41–43]. However, the observed ST rates are still far from an ideal value for alternative smart materials exhibiting up to picosecond phase transformations, conformations, thermal deformations, or defect formation for utilization as logic gates and switchers[44–46]. Nevertheless, we speculate that decreasing the dimension of MOFs (from bulk to nanosheets)[47] may contribute to an increased rates of ST and thermal deformations (heat propagation)[48–53].

Optical modulation

Generally, the ST (regardless of its nature) directly affects the electronic (optical) properties[40] and functionality of the solids[54–65]; hence, we have utilized the laser-induced thermal expansion of **1** to initiate its optical anisotropy for optical modulation. The ST scheme in Fig. 3a, expressed in the form of anisotropic change in the lattice parameters during the ST, predicts both an initial (before the ST, see Supplementary Fig. S22c) and the light-driven (during the ST) anisotropy of the optical properties of **1**. As we expected (Fig. 3b), the laser-induced heating with corresponding thermal expansion stimulated an anisotropic change in the refractive indices of single crystal of **1** at a fixed plane (for more details, see Methods and Supplementary Note 1, Supplementary Figs. S19, S20): A drop in the refractive index, n, by 1.3 % ($\Delta n = 0.02$) in (100) plane and by 0.7 % ($\Delta n = 0.01$) in (110) plane has been detected (see also Supplementary Fig. S23, S24). The observed changes of n are also in good agreement with the calculated data ($\Delta n = 0.005$) obtained for the structure of **1** heated from 298 to 338 K (Supplementary Table S12). Moreover, an analysis of the optical transmission of polarized light through the single crystal of **1** (of an arbitrary orientation) has revealed that rotating of the polarization of incoming light by 90° provides app. 3-fold increase in transmission (for the initial state of **1**, see Supplementary Figs. S18b, S20b–d). Herein, during the ST, this value equals to 9 (Supplementary Fig. S18b), which again proves that the ST induces an additional optical anisotropy of **1** (Supplementary Fig. S22c).

The observed effect of the ST on n values and the optical transmission of **1** in orthogonal directions brings us to an idea to rotate the polarization of visible light, passing through the single crystal of **1** with a thickness of 100 μm. This can be realized due to an unequal change in the optical transmission and n for the orthogonal components (like s and p as illustrated in Supplementary Figs. S23c, S24c) of the polarized light at 45° (for more details, see Supplementary Note 1). As can be seen in Fig. 3f (and Supplementary Fig. S22b–d), we have experimentally observed via two independent methods, that the polarization of light with a wavelength of 580 to 720 nm rotates additionally by 4°–30° (corresponding to app. 10^5 degree m^{-1})[66–72] from the initial position (i.e., 45°). Herein, an arbitrary (and uncontrolled) orientation of the single crystals of **1** with different thickness contributed to the values of determined rotation angles, as shown in Supplementary Fig. S22. Moreover, the direction of rotation of the polarization depends on the wavelength of light (Fig. 3f and Supplementary Fig. S22c): The orthogonal components of polarized light with a wavelength of 580-650 undergo unequally increased absorption during the ST (Supplementary Figs. S16b, S18b); while 650–720 nm light propagates in an opaque crystal, whose degree of transparency increases due to the ST. Taking into account the fact of the thickness of optically transparent crystals of **1** (10–100 μm), which minimized the contribution of the surface effect on the rotation of the polarization of visible light[73–75], the detected rotation by **1** (during the ST) in many respects exceeds such values for well-known optically active and anisotropic materials[63,66–72,75].

Finally, through the additional analysis of the ST by optical pump-probe spectroscopy with polarization resolution for the probing laser light (Supplementary Fig. S15), we have discovered a spatiotemporal dependence for the rates of the change of the MOF' optical properties (Fig. 3c, d): Again, comparing two orthogonal directions (0° and 90°) for the single crystals of **1** of an arbitrary orientation, we have revealed statistically the decrease in the excitation ST rate by 20 % (from $\kappa = 5000–4000\ s^{-1}$, corresponding to excitation time of 0.2 and 0.25 ms, respectively), and the decrease in the relaxation ST rate by 40% (corresponding to excitation time of 4–7 ms). This spatiotemporal process is also reflected in Fig. 3f (inset, and Supplementary Fig. S22a): the orthogonal components of polarized light (of 450 and 600 nm wavelengths), passing through **1**, demonstrate app. 0.1 ms time delay in their excitation and relaxation time relative to each other. According to our knowledge, this is the first observation of the anisotropic spatiotemporal behavior of the structure of coordination polymers (as previously observed for liquid crystals)[76,77], and can be explained by heat propagation thought the MOFs[48–53], complicated with their organic-inorganic nature, weak chemical bonding, and the structural anisotropy[53,78].

Conclusion

We report on a 2D MOF assembled from incomplete paddle-wheel secondary building units joined by a semi-flexible organic ligand with 1,2,4-triazole and carboxylate groups with a rigid adamantane cage between them. The structure results in a distinctive combination of the framework flexibility and endurance due to allowed deformations of the ligand shape and SBU in a reversible manner. It, thus, facilitates a continuous structural transformation, driven by low-intensity laser light. In situ optical, mechanical, numerical, and structural analysis reveal that such transformation is a laser-induced thermal expansion process, accompanied by reversible 1% anisotropic spatiotemporal volume expansion. We also confirm that the structural transformation initiates the change in optical properties of 2D MOF along orthogonal directions, utilized then for fast (5000 s^{-1}) and highly repeatable (over 10^4 cycles of ST) optical modulation. The latter is expressed as rotation of the polarization of the transmitted visible light. The reported endurance and structural resistance (during 1 year of storage at ambient conditions) of such 2D MOF-based optical modulator pave the way to design a series of tunable and robust MOFs for diverse chemical and optical applications[79–84] where transformation of the structure is required while maintaining its integrity[54–65].

Methods

Synthesis

The synthesis of MOF **1** was described in detail in ref. 37. Briefly, 2 ml of 0.1 M 3-(3-methyl-1,2,4-triazol-1-yl)-adamantane-1-carboxylic acid solution (0.2 mmol) in methanol was mixed with 1 ml 0.1 M solution (0.1 mmol) of copper(II) nitrate trihydrate in a 4 ml screwcap glass vial. The vial was placed in oven at 80 °C for 24 h. Upon cooling to room temperature, bright green crystals suitable for SCXRD analysis have been obtained, followed by their washing with 4 ml of methanol and storing under pure solvent.

Thermal gravimetric analysis (TGA) and differential scanning calorimetry (DSC)

TGA and DSC were performed on a NETZSCH TG 209 F1 Iris Thermo Microbalance from 30 to 850 °C (TGA) and 40 to 100 °C (DSC) under helium atmosphere with heating rate of 10 °C per min.

Single crystal XRD with heating mode

Variable-temperature single crystal XRD data were collected on a Bruker D8 Venture diffractometer with a CMOS PHOTON III detector and IμS 3.0 source (mirror optics, λ(MoKα) = 0.71073 Å). The φ- and ω-scan

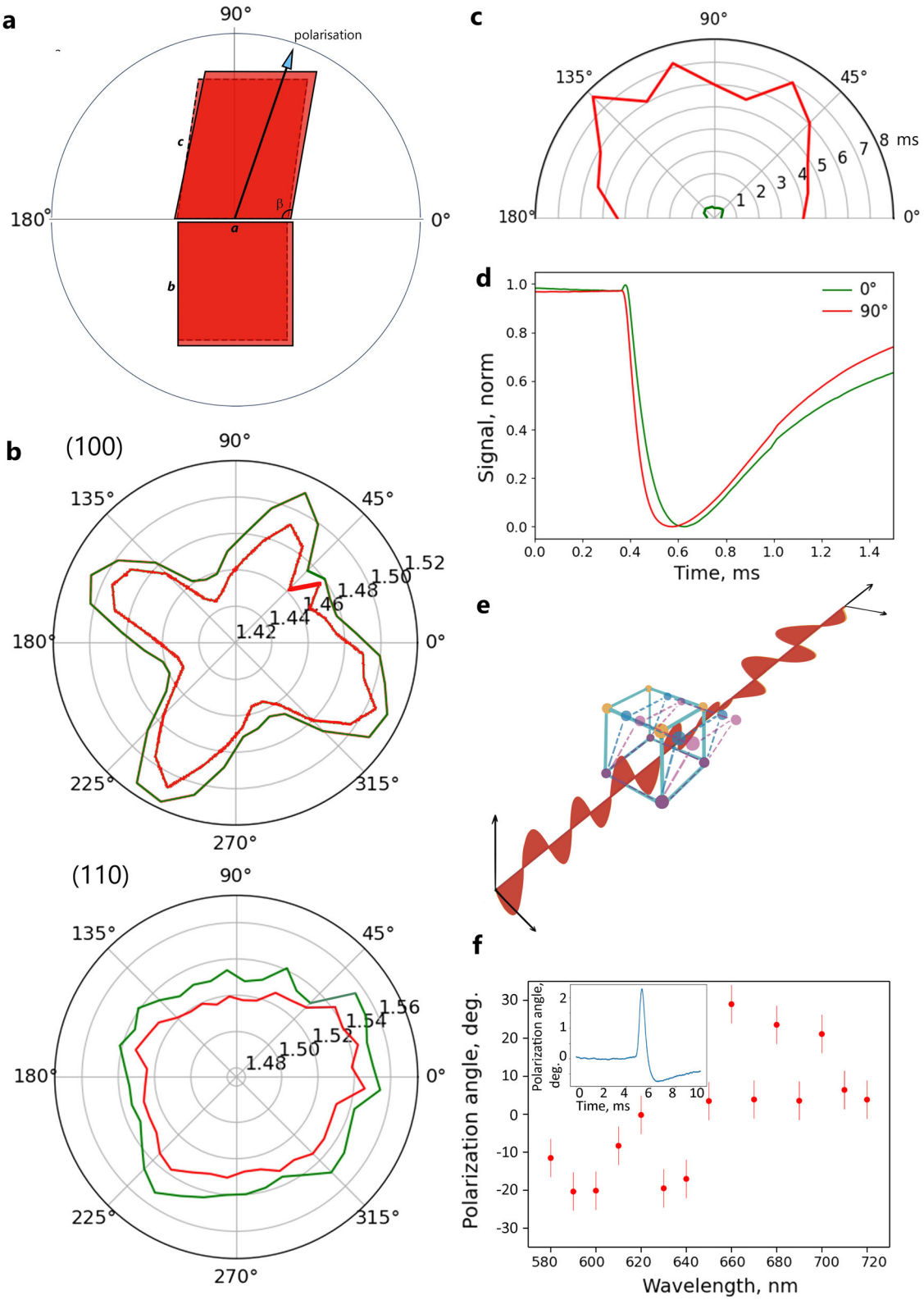

Fig. 3 | Optical anisotropy of 1 driven by the structural transformation. a A scheme of the ST of **1** in polar coordinates revealed by SCXRD (Supplementary Tables S1–S3). **b** Spatial dispersion of refractive index *n* for (100) and (110) planes of **1** (Supplementary Figs. S23, S24) before and during the ST, initiated by laser-induced heating (1050 nm, 4.5 mW of pumping laser power; green curve corresponds to the initial state, while the red one is for the excited state). **c**, **d** The dynamics of the ST expressed as the evolution of the intensity of 450 nm probing laser light with a varied polarization (0°–180°) passing through the single crystal of **1** during the ST, stimulated by a single 1064 nm (100 ns) laser pulse (red curve corresponds to the relaxation time in (**c**), while the green one is for the excitation time; green and red curves in (**d**) correspond to 0° and 90° polarization of the probing laser light). **e**, **f** Scheme and the experimentally measured rotation of the polarization of the probing laser light of a varied wavelength (580–720 nm, fluence of 0.28 mJ cm^{-2}) over time (inset) passing through the single crystal of **1** (of 100 μm thick and an arbitrary orientation) during the ST, stimulated by the laser irradiation (1050 nm, fluence of 3 mJ cm^{-2}).

techniques were employed to measure the intensities. The crystal structure was solved using the SHELXT and was refined using SHELXL programs with OLEX2 GUI. The corresponding references can be found in Supplementary Note 1. Atomic displacement parameters for non-hydrogen atoms were refined anisotropically, hydrogen atoms were placed geometrically and refined in the riding model.

In-situ powder XRD analysis with heating mode

Temperature-dependent powder X-ray diffraction was performed using a Rigaku Ultima IV diffractometer (CoKα radiation) equipped with a high-temperature camera. The MOF powder was ground on a platinum holder. The study was carried out in air in the temperature range of 298–338 K with a 5 K step and a heating rate of 1 K min^{-1} between the temperature points. The reflexes were recorded in the 2Θ range of 5–45°.

Single crystal XRD with laser mode

The XRD analyses were carried out using equipment of the Center for Joint Use "Spectroscopy and Analysis of Organic Compounds" at the Postovsky Institute of Organic Synthesis of the Russian Academy of Sciences (Ural Branch). The experiments were accomplished on the automated X-ray diffractometer «Xcalibur 3» with CCD detector on the standard procedure (MoKα-irradiation, graphite monochromator, ω-scans with 0.3° step for experiments at room temperature). The solution and refinement of the structures were accomplished by using Olex program package. Empirical absorption correction was applied. The structures were solved by the method of the intrinsic phases in SHELXT program and refined by SHELXL by the full-matrix least-squares method for non-hydrogen atoms. The H-atoms were placed in the calculated positions and were refined in the isotropic approximation. The laser irradiation of the single crystal of **1** during XRD experiments was accomplished by a laser source with 800 nm wavelength mounted in the safety chamber of the diffractometer. The single crystal was irradiated during the entire diffraction measurement procedure (up to 10 h) with 5 and 12 mW integral power focused by a lens (into 1 × 1 mm spot). The starting orientation of **1** in the axis of the goniometer from experiment to experiment did not change. The results of the XRD analyses in initial, excited (upon 5 and 12 mW irradiation), and reverse states are presented in Supplementary Table S7.

Molecular dynamics simulations

The thermal effect on **1** was estimated using molecular dynamics simulations at a constant number of particles, pressure, and temperature (NPT). The initial positions of the atoms were taken based on the crystallographic data. Universal Force Field (UFF), specifically its extension to MOFs, was used to describe the flexibility of the structure. The UFF force field was chosen due to its application to a variety of chemical elements and as well-established and widely used for simulations of different MOFs structures. Most importantly, this force field was shown previously to give a good description of the elastic properties of MOFs in a number of studies. Partial charges were not assigned to the atoms since their incorporation into a framework with the UFF force field produces worse agreement with experimental mechanical properties of MOFs. The simulations were performed in LAMMPS software. The structure was heated in a range of temperatures from 293 to 443 K. Lennard-Jones interactions were truncated at 12.5 Å. The Velocity-Verlet algorithm was used for time integration with a time step of 0.5 fs (which is typical for simulations of MOFs thermal behavior). Nosé-Hoover thermostat with 100 fs damping time and Nosé-Hoover barostat with 1000 fs damping time was used. Each temperature point included an equilibration time of 0.5 ns followed by a production time of 0.5 ns, where the average total energy of interactions was estimated.

Calculations of Raman spectrum and elastic constants

Periodic density functional theory (DFT) calculations have been performed in Kohn-Sham approach in CRYSTAL17 software (v.1.0.2). The initial structural data of the crystal of **1** with structural parameters for 298 and 338 K have been optimized in several ways: (i) with B3LYP functional (has been chosen due to less prominent change of cell parameters during the optimization process with respect to other functionals and optimization strategies) and fixed volume for the calculations of elastic constant tensor; (ii) with PBEh-3c/PBE0 functional with fixed cell parameters for the calculation of Raman active modes and their intensities. Such combination with the implementation of three-fold corrected (3c) Hartree-Fock method together with classical PBE0 approach has been chosen in order to accelerate the calculation speed due to large number of atoms in the unit cell (492 atoms), which is especially important in the calculation of frequencies. Basis set was unified for all of the calculations: the 6–31 G(d) basis set for the H, C, N, O atoms and basis set for the Cu atoms (see details in Supplementary Note 1). Calculation of Raman active modes has been done in couple-perturbed Kohn-Sham approach for both 298 and 338 K cases. Calculation of elastic constants tensor has been applied for the optimized structure of **1** at 298 K with relaxed cell parameters and fixed cell volume. The spatial dependences of elastic moduli were calculated from stiffness tensors by means of the ELATE online tool. This tool also allowed us to calculate the tensor eigenvalues, the minimum and maximum values of Young's modulus and linear compressibility, as well as the directions of their extremal values (see Supplementary Figs. S11–S13).

Transmission optical spectroscopy with heating and laser modes

A homemade setup based on confocal microscopy spectrometer HORIBA Labram with water cooling Andor VIS/NIR cameras and diffraction gratings kit (150 and 1800 g mm^{-1}) has been used for MOF characterization. The setup was reconfigurable and allowed us to provide a series of optical experiments with spectral, spatial, and time resolution involving mechanical shutter for laser selection, infinity-corrected objectives, and sample heating tool. As pump sources, two lasers were used: 800 nm diode continuous wave laser with external resonator (model ECDL-7930R) and 1050 nm Yb^{3+} doped femtosecond laser TEMA (150 fs pulse duration, 80 MHz repetition rate). A Mitutoyo NIR 10 × 0.28NA objective was installed in the excitation channel, and a Mitutoyo VIS 50 × 0.56NA objective was used in the collection channel. The effect of the optical spectral shift was confirmed for both sources and correlated with the absorption band of the crystal spectra transmission (Supplementary Fig. S14). The optical transmission experiment with heating has been provided using a resistive heater with stabilization close-loop that allowed stabilizing the temperature in the range from 25 to 100 °C with accuracy ±1 °C. The analysis of the spectral shift from obtained data was discussed in detail in Supplementary Note 1.

Transmission optical spectroscopy with polarization resolution

The polarization transmission optical spectroscopy has been implemented for the estimation of the change in rotation angle for a polarized white light (Supplementary Fig. S22c, d). For this, the single crystals of **1** were settled on a glass substrate. A Mitutoyo NIR 10x0.26NA objective was installed in the excitation channel (to initiate the ST), and a Mitutoyo VIS 50x0.55NA objective was used in the collection channel. A polarization vector from the white light (Avantes 300–2500 lamp) has 45° polarization after passing throw the Glan prism and half wave plate. After the passing through the excited crystal, the signal passed through the Glan prism in two orthogonal positions in order to detect two orthogonal components (*s* and *p* polarized signals) of a white polarization light and then was analyzed by spectrometer HORIBA Labram with water cooling Andor VIS/NIR cameras and diffraction gratings kit (150 and 1800 g mm^{-1}). As pump source for initiating the ST, 1050 nm Yb^{3+} doped femtosecond laser TEMA (150 fs pulse duration, 80 MHz repetition rate) was used.

Pump-probe spectroscopy with a time resolution

The pump-probe optical spectroscopy approach with time resolution has been implemented for estimation the timing parameters of the optical transmission spectra. A supercontinuum source (Fianium picosecond laser, 60 MHz pulse repetition rate, 6 ps pulse duration, passed through the tunable spectral filter SuperChrome to select 500–750 nm) was used to generate a probe laser light. A commercially available Yb^{3+} doped fiber laser

(IPG Photonics) operating at wavelength of 1064 nm, with 100 ns pulse duration, and repetition rate of 1.6 kHz was as a pump laser; to decrease the pulse repetition rate, a chopper-based modulator Thorlabs MC2000B with an MC1F60 blade that transmits radiation in one of 60 slots was implemented and synchronized by frequency and phase with a nanosecond laser based on a photodetector signal. The probe signal was detected using high-speed photodetector Standa 11HSP-FS1 and analyzed then using an oscilloscope.

Pump-probe spectroscopy with polarization resolution

The polarization-resolved pump-probe optical spectroscopy has been implemented for the estimation the timing parameters of the optical transmission spectra for a polarized probe laser light (Supplementary Fig. S15). For this, the single crystals of **1** were settled on a glass substrate. A Mitutoyo NIR 10x0.26NA objective was installed in the excitation channel (to initiate the ST), and a Mitutoyo VIS 100x0.9NA objective was used in the collection channel. A signal from supercontinuum source (Fianium picosecond laser, 60 MHz pulse repetition rate, 6 ps pulse duration, 200 μW integral power) passed through a tunable visible spectral filter (SuperChrome the spectral range 400–800 nm, FWHM 10 nm, 6 ns pulse duration), was used as a probe source. As a pump source, a commercially available Yb^{3+} doped femtosecond laser (wavelength of 1050 nm, with 150 fs pulse duration, 80 MHz repetition rate, and a fluence of 3 mJ cm^{-2}) was used; to select the chain of femtosecond pulses, a chopper-based modulator Thorlabs MC2000B with an MC1F60 blade that transmits radiation in one of 60 slots was implemented, the radiation to which was diverted using a beam-splitting cube. The polarization vector of probe beam has 45° polarization after passing throw the Glan prism and half wave plate. The pump beam was analyzed than using the signal from the photodetector settled in the excitation channel and was cut off using a short-pass visible spectral filter; while the probe light was detected in a balanced scheme including a polarization beam splitter cube and two high-speed photodetectors (rising time less than 1 ns), and an oscilloscope, which provides detection of two orthogonal components (*s* and *p* polarized signals in Supplementary Fig. S22a) of probe polarization light. The estimation of the angle of the rotation of polarization vector over time is presented in details in Supplementary Note 1.

Endurance

The stability of switching between initial and excited states has been provided in the scheme described in Supplementary Fig. S14, with additional irradiation of 1050 nm femtosecond laser. The white light transmitted through the single crystals of **1** of an arbitrary orientation was detected by a commercial spectrometer Avantes in the visible spectral range. The mechanical shutter was opened and closed laser irradiation that allowed detecting an initial and exciting state in each iteration. The shift was calculated as a difference of wavelength positions with an accuracy of 0.005 nm for fixed intensity on each iteration. Two crystals of **1** were considered as a model object including a 1-year stay in the air crystal (the old one in Supplementary Fig. S25) and another crystal dried from matrix solvent (the new one in Fig. 2c and Supplementary Fig. S26). The fluence of the 1050 nm laser source was 2.4 mJ cm^{-2} for the old crystal, and 3.6 mJ cm^{-2} for the new one.

Refractive index analysis

To analyze the refractive indices, *n*, of the single crystals of **1** (of an arbitrary orientation, Supplementary Figs. S19, S20, and determined orientation, Supplementary Figs. S23, S24), we have measured the reflectance spectra depending on the angle of polarization of incoming light (Supplementary Fig. S19). For this, the single crystals of **1** were settled on a glass substrate. A Mitutoyo NIR 10x0.26NA objective was installed in the excitation channel (to initiate the ST by 1050 nm laser light with 4.5 mW power), and a Mitutoyo VIS 100x0.9NA objective was used in the collection channel. A signal from white light source (Avantes 300–2100 nm spectral range lamp) reflected from the MOF surface via collection channel, the Glan prism, and a half-wave plate with a step of 10°, have been analyzed with a spectrometer (AvaSpec-ULS2048CL-EVO). The mathematical analysis of the refractive index and its changes (during the ST, initiated by laser-induced heating) is presented in Supplementary Note 1.

Raman spectroscopy

Raman spectra (Supplementary Fig. S27) have been measured using a triple spectrometer T64000 (Horiba, Jobin Yvon) in subtraction dispersion mode. As a light source, an DPSS laser Spectra-Physics Excelsior-532-300-CDRH at a wavelength of 532 nm has been used. Signal accumulation time was set at 960 s, with 2 cm^{-1} spectral resolution, 0.3 cm^{-1}CCD matrix pixel coverage, and 1 mW laser excitation power. The laser beam was focused by a lens with a large working distance 10.5 mm of 50× (NA 0.5). The scattered light was collected by the same lens in the backscattering geometry. Thermal measurement of individual MOF crystals was investigated using a temperature-controlled stage THMS600 (Linkam Sci. Inst.). The MOF has been heated in the range from 22 °C to 180 °C with a constant heating rate of 5 °C per minute. After reaching a certain point value, the temperature remained constant, and the Raman spectra have been measured after 10 min (required for uniform heating). Additionally, the unfocused beam with 300 μm diameter from the red laser pointer with a wavelength of 650 nm illuminated the MOF. The angle between the green Raman laser and the red one was set at 60°.

Mechanical characterization

Mechenical characteristics have been estimated using atomic force microscopy (SmartSPM 1000 AIST-NT microscope) in contact mode at ambient conditions. Working cantilevers were PPP-NCSTAuD-10 (Nanosensors) with 160 kHz resonance frequency, 14 N m^{-1} force constant, and 10 nm tip radius of curvature; CP-qp-SCONT-SiO-A (sQube) cantilevers with round tip made of silicon dioxide with diameter of 2 μm, and 0.01 N m^{-1} force constant.

Data availability

The X-ray crystallographic coordinates for structures reported in this Article have been deposited at the Cambridge Crystallographic Data Centre (CCDC), under deposition numbers CCDC 2278066 (at 298 K) and 2278067 (at 338 K) and 2312382-2312386 (for gradual heating). These data can be obtained free of charge from The Cambridge Crystallographic Data Centre via www.ccdc.cam.ac.uk/data_request/cif.

Received: 25 July 2023; Accepted: 29 March 2024;
Published online: 10 April 2024

References

1. Rieth, A. J., Wright, A. M. & Dincă, M. Kinetic stability of metal–organic frameworks for corrosive and coordinating gas capture. *Nat. Rev. Mater.* **4**, 708–725 (2019).
2. Knebel, A. et al. Defibrillation of soft porous metal-organic frameworks with electric fields. *Science* **358**, 347–351 (2017).
3. Mezenov, Y. A. et al. Polymer matrix incorporated with ZIF-8 for application in nonlinear optics. *Nanomaterials* **10**, 1036 (2020).
4. Evans, J. D., Bon, V., Senkovska, I., Lee, H.-C. & Kaskel, S. Four-dimensional metal-organic frameworks. *Nat. Commun.* **11**, 2690 (2020).
5. Schneemann, A. et al. Flexible metal–organic frameworks. *Chem. Soc. Rev.* **43**, 6062–6096 (2014).
6. Horike, S., Shimomura, S. & Kitagawa, S. Soft porous crystals. *Nat. Chem.* **1**, 695–704 (2009).
7. Chang, Z., Yang, D.-H., Xu, J., Hu, T.-L. & Bu, X.-H. Flexible metal–organic frameworks: recent advances and potential applications. *Adv. Mater.* **27**, 5432–5441 (2015).
8. Senkovska, I. et al. Understanding MOF flexibility: an analysis focused on pillared layer MOFs as a model system. *Angew. Chem. Int. Ed.* **62**, e202218076 (2023).

9. Meng, W. et al. An elastic metal–organic crystal with a densely catenated backbone. *Nature* **598**, 298–303 (2021).
10. Ehrling, S. et al. Adaptive response of a metal–organic framework through reversible disorder–disorder transitions. *Nat. Chem.* **13**, 568–574 (2021).
11. Katsoulidis, A. P. et al. Chemical control of structure and guest uptake by a conformationally mobile porous material. *Nature* **565**, 213–217 (2019).
12. Carrington, E. et al. Solvent-switchable continuous-breathing behaviour in a diamondoid metal–organic framework and its influence on CO2 versus CH4 selectivity. *Nat. Chem.* **9**, 882–889 (2017).
13. Kulachenkov, N. et al. Dimensionality mediated highly repeatable and fast transformation of coordination polymer single crystals for all-optical data processing. *Nano Lett.* **22**, 6972–6981 (2022).
14. Kulachenkov, N. K. et al. Photochromic free MOF-based near-infrared optical switch. *Angew. Chem. Int. Ed.* **59**, 15522 (2020).
15. Bigdeli, F., Lollar, C. T., Morsali, A. & Zhou, H.-C. Switching in metal–organic frameworks. *Angew. Chem. Int. Ed.* **59**, 4652 (2020).
16. Rice, A. M. et al. Photophysics modulation in photoswitchable metal–organic frameworks. *Chem. Rev.* **120**, 8790–8813 (2020).
17. Zeng, H. et al. Orthogonal-array dynamic molecular sieving of propylene/propane mixtures. *Nature* **595**, 542–548 (2021).
18. Liu, J. et al. Smart covalent organic networks (CONs) with “on-off-on” light-switchable pores for molecular separation. *Sci. Adv.* **6**, eabb3188 (2020).
19. Lin, R.-B., Xiang, S., Zhou, W. & Chen, B. Microporous metal-organic framework materials for gas separation. *Chem* **6**, 337–363 (2020).
20. Canossa, S., Ji, Z. & Wuttke, S. Circumventing wear and tear of adaptive porous materials. *Adv. Funct. Mater.* **30**, 1908547 (2020).
21. Sato, O. Dynamic molecular crystals with switchable physical properties. *Nat. Chem.* **8**, 644–656 (2016).
22. Turner, G. F. et al. Guest-mediated phase transitions in a flexible pillared-layered metal–organic framework under high pressure. *Chem. Sci.* **12**, 13793–13801 (2021).
23. Lyu, J. et al. Phase transitions in metal–organic frameworks directly monitored through in situ variable temperature liquid-cell transmission electron microscopy and in situ X-ray diffraction. *J. Am. Chem. Soc.* **142**, 4609–4615 (2020).
24. Pallach, R. et al. Frustrated flexibility in metal-organic frameworks. *Nat. Comm.* **12**, 4097 (2021).
25. Zhang, J., Kosaka, W., Kitagawa, Y. & Miyasaka, H. A metal–organic framework that exhibits CO2-induced transitions between paramagnetism and ferrimagnetism. *Nat. Chem.* **13**, 191–199 (2021).
26. Perego, J. et al. Fast motion of molecular rotors in metal–organic framework struts at very low temperatures. *Nat. Chem.* **12**, 845–851 (2020).
27. Danowski, W. et al. Unidirectional rotary motion in a metal–organic framework. *Nat. Nanotechnol.* **14**, 488–494 (2019).
28. Guillerm, V., Grancha, T., Imaz, I., Juanhuix, J. & Maspoch, D. Zigzag ligands for transversal design in reticular chemistry: unveiling new structural opportunities for metal–organic frameworks. *J. Am. Chem. Soc.* **140**, 10153–10157 (2018).
29. Yang, L. et al. Ligand-directed conformational control over porphyrinic zirconium metal–organic frameworks for size-selective catalysis. *J. Am. Chem. Soc.* **143**, 12129–12137 (2021).
30. Bennett, T. D. & Horike, S. Liquid, glass and amorphous solid states of coordination polymers and metal–organic frameworks. *Nat. Rev. Mater.* **3**, 431–440 (2018).
31. Kulachenkov, N. et al. MOF-based sustainable memory devices. *Adv. Funct. Mater.* **32**, 2107949 (2022).
32. Chen, X., Gao, H., Tang, Z. & Wang, G. Metal-organic framework-based phase change materials for thermal energy storage. *Cell Rep. Phys. Sci.* **1**, 100218 (2020).
33. Meekel, E. G. et al. Truchet-tile structure of a topologically aperiodic metal–organic framework. *Science* **379**, 357–361 (2023).
34. Alekseevskiy, P. V. et al. Flexible metal-organic framework for mechanical sub Tbyte inch−2 data recording under ambient condition. *Adv. Mater. Interfaces* **8**, 2101196 (2021).
35. Barker, R. E. Jr An approximate relation between elastic moduli and thermal expansivities. *J. Appl. Phys.* **34**, 107–116 (1963).
36. Henke, S., Schneemann, A. & Fischer, R. A. Massive anisotropic thermal expansion and thermo-responsive breathing in metal–organic frameworks modulated by linker functionalization. *Adv. Funct. Mater.* **23**, 5990–5996 (2013).
37. Pavlov, D., Sukhikh, T., Filatov, E. & Potapov, A. Facile synthesis of 3-(Azol-1-yl)-1-adamantanecarboxylic acids—new bifunctional angle-shaped building blocks for coordination polymers. *Molecules* **24**, 2717 (2019).
38. Zhang, W. et al. Reconstructed covalent organic frameworks. *Nature* **604**, 72–79 (2022).
39. Horstmann, J. G. et al. Coherent control of a surface structural phase transition. *Nature* **583**, 232–236 (2020).
40. Pattengale, B., Ostresh, S. & Schmuttenmaer, C. A. Interrogating light-initiated dynamics in metal–organic frameworks with time-resolved spectroscopy. *Chem. Rev.* **122**, 132–166 (2022).
41. Sheberla, D. et al. Conductive MOF electrodes for stable supercapacitors with high areal capacitance. *Nat. Mater.* **16**, 220–224 (2017).
42. Ding, G. et al. 2D metal–organic framework nanosheets with time-dependent and multilevel memristive switching. *Adv. Funct. Mater.* **29**, 1806637 (2019).
43. Pan, L. et al. Metal-organic framework nanofilm for mechanically flexible information storage applications. *Adv. Funct. Mater.* **25**, 2677–2685 (2015).
44. Hase, M., Fons, P., Mitrofanov, K., Kolobov, A. V. & Tominaga, J. Femtosecond structural transformation of phase-change materials far from equilibrium monitored by coherent phonons. *Nat. Commun.* **6**, 8367 (2015).
45. Abdollahramezani, S. et al. Electrically driven reprogrammable phase-change metasurface reaching 80% efficiency. *Nat. Commun.* **13**, 1696 (2022).
46. Liu, S. et al. An ultrasmall organic synapse for neuromorphic computing. *Nat. Commun.* **14**, 7655 (2023).
47. Efimova, A. S. et al. Exfoliation of 2D metal-organic frameworks: toward advanced scalable materials for optical sensing. *Small Methods* **11**, 2300752 (2023).
48. Babaei, H. et al. Observation of reduced thermal conductivity in a metal-organic framework due to the presence of adsorbates. *Nat. Commun.* **11**, 4010 (2020).
49. Sezginel, K. B., Asinger, P. A., Babaei, H. & Wilmer, C. E. Thermal transport in interpenetrated metal–organic frameworks. *Chem. Mater.* **30**, 2281–2286 (2018).
50. Babaei, H., McGaughey, A. J. H. & Wilmer, C. E. Effect of pore size and shape on the thermal conductivity of metal-organic frameworks. *Chem. Sci.* **8**, 583–589 (2017).
51. Hoffman, A. E. J. et al. The role of phonons in switchable MOFs: a model material perspective. *J. Mater. Chem. A* **11**, 15286–15300 (2023).
52. Qian, X., Zhou, J. & Chen, G. Phonon-engineered extreme thermal conductivity materials. *Nat. Mater.* **20**, 1188–1202 (2021).
53. Evans, A. M. et al. Thermally conductive ultra-low-k dielectric layers based on two-dimensional covalent organic frameworks. *Nat. Mater.* **20**, 1142–1148 (2021).
54. Wuttig, M., Bhaskaran, H. & Taubner, T. Phase-change materials for non-volatile photonic applications. *Nat. Photon* **11**, 465–476 (2017).
55. Zhang, W., Mazzarello, R., Wuttig, M. & Ma, E. Designing crystallization in phase-change materials for universal memory and neuro-inspired computing. *Nat. Rev. Mater.* **4**, 150–168 (2019).

56. Yanai, N. et al. Guest-to-host transmission of structural changes for stimuli-responsive adsorption property. *J. Am. Chem. Soc.* **134**, 4501–4504 (2012).
57. Mason, J. A. et al. Methane storage in flexible metal–organic frameworks with intrinsic thermal management. *Nature* **527**, 357–361 (2015).
58. Shen, P. et al. Solid-state structural transformation doubly triggered by reaction temperature and time in 3D metal-organic frameworks: great enhancement of stability and gas adsorption. *Chem. Sci.* **5**, 1368–1374 (2014).
59. Jiang, Y. et al. Crystal transformation in Mn(ii) metal–organic frameworks based on a one-dimensional chain precursor. *Dalton Trans.* **50**, 9540–9546 (2021).
60. Yao, Z.-Q. et al. Dynamic full-color tuning of organic chromophore in a multi-stimuli-responsive 2D flexible MOF. *Angew. Chem. Int. Ed.* **61**, e202202073 (2022).
61. Wu, Z.-F. et al. Achieving a blue-excitable yellow-emitting CaLMOF phosphor via water induced phase transformation. *Chem. Sci.* **13**, 1375–1381 (2022).
62. Jiang, H.-L., Tatsu, Y., Lu, Z.-H. & Xu, Q. Non-, micro-, and mesoporous metal−organic framework isomers: reversible transformation, fluorescence sensing, and large molecule separation. *J. Am. Chem. Soc.* **132**, 5586–5587 (2010).
63. Vinogradov, A. V. et al. Unique anisotropic optical properties of a highly stable metal–organic framework based on trinuclear iron(III) secondary building units linked by tetracarboxylic linkers with an anthracene core. *Dalton Trans.* **45**, 7244–7249 (2016).
64. Zhestkij, N. et al. Reversible and irreversible laser interference patterning of MOF thin films. *Crystals* **12**, 846 (2022).
65. Bachinin, S., Marunchenko, A., Zhestkij, N., Gunina, E. & Milichko, V. A. Metal-organic framework single crystal infrared photodetector. *Photon. Nanostruct. Fund. Appl.* **55**, 101145 (2023).
66. Minkovski, N., Petrov, G. I., Saltiel, S. M., Albert, O. & Etchepare, J. Nonlinear polarization rotation and orthogonal polarization generation experienced in a single-beam configuration. *J. Opt. Soc. Am. B* **21**, 1659–1664 (2004).
67. Jullien, A. et al. Nonlinear polarization rotation of elliptical light in cubic crystals, with application to cross-polarized wave generation. *J. Opt. Soc. Am. B* **22**, 2635–2641 (2005).
68. Ren, M., Plum, E., Xu, J. & Zheludev, N. I. Giant nonlinear optical activity in a plasmonic metamaterial. *Nat. Commun.* **3**, 833 (2012).
69. Kuwata-Gonokami, M. et al. Giant optical activity in quasi-two-dimensional planar nanostructures. *Phys. Rev. Lett.* **95**, 227401 (2005).
70. Franklin, D., Frank, R., Wu, S.-T. & Chanda, D. Actively addressed single pixel full-colour plasmonic display. *Nat. Commun.* **8**, 15209 (2017).
71. Ganeev, R. A. et al. Nonlinear optical characteristics of BSO and BGO photorefractive crystals in visible and infrared ranges. *Opt. Quant. Electr.* **36**, 807–818 (2004).
72. Kundrat, M. D. & Autschbach, J. Computational modeling of the optical rotation of amino acids: a new look at an old rule for pH dependence of optical rotation. *J. Am. Chem. Soc.* **130**, 4404–4414 (2008).
73. Liang, J. H. et al. Quantitative study of the quadratic magneto-optical Kerr effects in Fe films. *Opt. Express* **23**, 11357–11366 (2015).
74. Rowan-Robinson, R. M. et al. Thickness dependent enhancement of the polar Kerr rotation in Co magnetoplasmonic nanostructures. *AIP Adv.* **9**, 025317 (2019).
75. Sabatini, R. P. et al. Solution-processed faraday rotators using single crystal lead halide perovskites. *Adv. Sci.* **7**, 1902950 (2020).
76. Chen, X., Korblova, E., Glaser, M. A. & Clark, N. A. Polar in-plane surface orientation of a ferroelectric nematic liquid crystal: polar monodomains and twisted state electro-optics. *Proc. Nat. Acad. Sci.* **118**, e2104092118 (2021).
77. Cattaneo, L., Savoini, M., Muševič, I., Kimel, A. & Rasing, T. Ultrafast all-optical response of a nematic liquid crystal. *Opt. Express* **23**, 14010–14017 (2015).
78. Kim, S. E. et al. Extremely anisotropic van der Waals thermal conductors. *Nature* **597**, 660–665 (2021).
79. Yu, J. et al. Metal−organic framework-based ultrafast logic gates for high-security optical encryption. *Ultrafast Sci.* **3**, 0030 (2023).
80. Milichko, V. A. et al. van der Waals metal-organic framework as an excitonic material for advanced photonics. *Adv. Mater.* **29**, 1606034 (2017).
81. Zheng, H.-Q. et al. Photo-stimuli-responsive dual-emitting luminescence of a spiropyran-encapsulating metal–organic framework for dynamic information encryption. *Adv. Mater.* **35**, 2300177 (2023).
82. Xie, Y., Sun, G., Li, J., Sun, L. Multimode emission from lanthanide-based metal–organic frameworks for advanced information encryption. *Adv. Funct. Mater*. **33**, 2303663 (2023).
83. Kenzhebayeva, Y. et al. Light-induced color switching of single metal–organic framework nanocrystals. *J. Phys. Chem. Lett.* **13**, 777–783 (2022).
84. Mingabudinova, L. R., Vinogradov, V. V., Milichko, V. A., Hey-Hawkins, E. & Vinogradov, A. V. Metal–organic frameworks as competitive materials for non-linear optics. *Chem. Soc. Rev.* **45**, 5408–5431 (2016).

Acknowledgements

V.A.M. acknowledges the financial support from the Russian Science foundation (Grant Numb. 22-72-10027 “Flexible hybrid materials as active layer in memory devices”, work on pump-probe and nonlinear optical spectroscopuy) and the Priority 2030 Federal Academic Leadership Program. Y.A.K. acknowledges the financial support from the Russian Science foundation (Grant Numb. 19-79-10259 for transmission optical spectroscopy with heating and laser mode). S.S. acknowledges the financial support by the Government of the Russian Federation through the ITMO Fellowship and Professorship Program. P.A. acknowledge AFM Centre of ITMO University for help with the MOF mechanical characterization. Temperature-dependent SCXRD analysis was carried out at XRD facilities of NIIC operating with the support from the Ministry of Science and Higher Education of the Russian Science Federation (project 121031700321-3). The authors would like to thank Mirko Schoenitz and Irina Molodetsky for discussion of crystallographic data. A.K. acknowledges the financial support from RFBR and DFG (Grant Numb. 21-52-12018 for Raman measurements). Raman experiments have been performed in the Center of Common Use of the Krasnoyarsk Scientific Center SB RAS.

Author contributions

V.A.M. designed the concept. V.A.M. and A.S.P. designed the study and supervised the project. Y.A.K. and N.K.K. performed the most optical experiments. S.S.R. designed the setup for an endurance measurement. A. Efimova and P.A. performed mechanical measurements. G.Y.G. and A. Emelianova performed molecular modeling. I.D.Y. reformed mechanical, Raman, and refractive index modeling. A.K. performed Raman spectroscopy. D.I.P., V.P.F. and A.S.P. designed the MOF structure and performed most structural analysis. P.A.S. and S.S. performed additional structural analysis. V.V.S. assisted in sample preparation for mechanical and endurance measurements. All the authors discussed the results of this article.

Competing interests

The authors declare no competing interests.

Additional information

Supplementary information For methods, see Supplementary Note 1; for the structural analysis see Supplementary Notes 2 and 3, Supplementary Tables S1–S7, Supplementary Figures S1–S5, and cif files Supplementary

Data 1 (CCDC 2278088, at 298 K), Supplementary Data 2 (CCDC 2312382, at 298 K), Supplementary Data 3 (CCDC 2312383, at 308 K), Supplementary Data 4 (CCDC 2312384, at 318 K), Supplementary Data 5 (CCDC 2312385, at 328 K), Supplementary Data 6 (CCDC 2312386, at 338 K), and Supplementary Data 7 (CCDC 2278067, at 338 K); for molecular modeling see Supplementary Note 4, Supplementary Table S8, Supplementary Figure S6, and Supplementary Video 1; for mechanics, see Supplementary Notes 5 and 6, Supplementary Tables S9–S11, Supplementary Figures S7–S13; for additional optical results, see Supplementary Note 7, Supplementary Tables S12, S13, and Supplementary Figures S14–S27. The online version contains supplementary material available at https://doi.org/10.1038/s43246-024-00485-5.

Correspondence and requests for materials should be addressed to Andrei S. Potapov or Valentin A. Milichko.

Peer review information *Communications Materials* thanks Tom Roseveare and the other, anonymous, reviewer(s) for their contribution to the peer review of this work. Primary Handling Editors: Jet-Sing Lee. A peer review file is available.